

EFFECT OF NICKEL CONTENT ON THE CRYSTALLIZATION BEHAVIOR  
IN NANOCRYSTALLINE  $(CO_{1-x}Ni_x)_{88}ZR_7B_4CU_1$   
SOFT MAGNETIC ALLOYS

by

BILLY CHAD HORNBUCKLE

GREGORY B. THOMPSON, COMMITTEE CHAIR

NITIN CHOPRA

GARY MANKEY

A THESIS

Submitted in partial fulfillment of the requirements for the degree  
of Master of Science in the Department of  
Metallurgical and Materials Engineering  
in the Graduate School of  
The University of Alabama

TUSCALOOSA, ALABAMA

2012

Copyright Billy Chad Hornbuckle 2012

ALL RIGHTS RESERVED

## ABSTRACT

A series of  $(Co_{1-x}Ni_x)_{88}Zr_7B_4Cu_1$  soft magnetic alloys, where X was varied from 0 to 1, were fabricated by a melt spinning process into thin ribbons of the material. This process was followed by an isothermal anneal to produce a nanocomposite alloy, i.e. nanocrystalline grains in a residual amorphous matrix. The alloy series was designed to investigate crystallization kinetics and limits to the compositional regime where a nanocomposite could be formed. The primary and secondary crystallization temperatures of each alloy were determined using Differential Scanning Calorimetry (DSC) from which the crystallization activation energies were calculated using the Kissinger Method. When X exceeded 0.75, the as-spun ribbons exhibited partial crystallization, resulting in reduced exothermic crystallization peaks. For lower Ni contents, the ribbons were amorphous in the as-spun state. The activation energy for crystallization decreased with increasing Ni content.

Transmission Electron Microscopy (TEM) and Atom Probe Tomography (APT) revealed fine nanocrystallite and boron segregation to the grain boundaries with increasing Ni content. The previously suspected use of Cu clustering, which can act as heterogeneous nucleation sites, showed no clear correlation with observed spatial location of the crystallites.

Chemical partitioning between species in the as-spun and primary crystallization heat treatments were correlated to the resulting changes in magnetic properties. As Ni content increased, the saturation magnetization and normalized magnetization for these samples decreased accordingly.



## LIST OF ABBREVIATIONS AND SYMBOLS

AC	Alternating Current
at.%	Atomic percent
APT	Atom Probe Tomography
A2	Body centered cubic crystal with Im-3m space grouping
B2	Body centered cubic crystal with Pm-3m
cm	Centimeters
°C	Celsius
D	Grain size
DC	Direct Current
DSC	Differential Scanning Calorimetry
<i>et al.</i>	And others
fcc	Face centered cubic
FIB	Focused ion beam
GIS	Gas Injection System
HAADF	High angle annular dark field

hcp	Hexagonal close packed
$\Delta H_{\text{mix}}$	Enthalpy of mixing
IVAS	Integrated Visualization & Analysis Software
K	Kelvins
keV	Kilo-electron volts
kHz	Kilo-Hertz
kJ	Kilo-Joules
kOe	Kilo-Oersted
$K_1$	Anisotropy constant
LEAP	Local Electrode Atom Probe
ln	Natural logarithm
m	Meters
mA	Micro-Ampere
$\mu\text{m}$	Micron (micrometer)
mil	A thousandth of an inch
mm	Millimeter
mol	Moles

nJ	Nano-Joule
nm	Nanometer
Q	Activation Energy
s	Seconds
SAED	Selected Area Electron Diffraction
SEM	Scanning Electron Microscope
STEM	Scanning Transmission Electron Microscope
$T_c^{am}$	Curie temperature of amorphous phase
TEM	Transmission electron microscope
$T_p$	Primary crystallization temperature
$T_{p-20}$	20°C below primary crystallization temperature
$T_{p+50}$	50°C below primary crystallization temperature
VSM	Vibrating Sample Magnetometry
wt.%	Weight percent
XRD	X-ray diffraction

## ACKNOWLEDGMENTS

I would like to thank my parents, brother, and the rest of my family for their love and support as my educational journey continued into graduate school. First and foremost, I would be remiss if I did not thank my advisor Dr. Gregory Thompson, the chairman of this thesis, for giving me my first opportunity to perform research during my undergraduate career and allowing me to continue on under his guidance during my graduate studies. I would like to thank Drs. Karen Torres Henry, Robb Morris, Taisuke Susaki, and Billie Wang for the hours of tutelage they spent on teaching me how to properly perform research, training me on the usage of all the varying tools, and honing my technical writing. I would like to thank my committee members, Dr. Nitin Chopra and Dr. Gary Mankey for their invaluable input, questions, and support for my thesis and my overall academic progress. Finally, I would like to thank Drs. Matt Willard and Maria Daniil for the opportunity to melt-spin the ribbons and perform the magnetic measurements during my internship at the Naval Research Laboratory. Their advice and knowledge was invaluable. With regard to the financing, this work has been partially supported by NSF-DMR-0547445 and the remainder coming from the Office of Naval Research Laboratory (ONRL) Summer Employment Program.

Once again, I would like to emphasize my appreciation for the support of my family, friends, and fellow graduate students.

## CONTENTS

ABSTRACT.....	II
LIST OF ABBREVIATIONS AND SYMBOLS .....	IV
ACKNOWLEDGMENTS .....	VII
LIST OF TABLES.....	X
LIST OF FIGURES .....	XI
CHAPTER 1 INTRODUCTION.....	1
1.1 SOFT MAGNETIC MATERIALS.....	1
1.2 AMORPHOUS MATERIALS.....	2
1.3 NANOCRYSTALLINE SOFT MAGNETIC MATERIALS.....	3
1.3.1 Nanocrystalline Soft Magnetic Materials .....	3
1.3.2 FINEMET / VITROPERM .....	4
1.3.3 NANOPERM .....	5
1.3.4 HITPERM .....	5
1.3.5 Microstructure Engineering Magnetic Nanocrystalline and Amorphous Alloys ....	6
CHAPTER 2 EXPERIMENTAL .....	8
2.1 MELT-SPINNING PROCESSING .....	8
2.2 DIFFERENTIAL SCANNING CALORIMETRY (DSC).....	11
2.3 ENCAPSULATIONS AND HEAT TREATMENT .....	12
2.4 MAGNETIC PROPERTIES MEASUREMENT .....	13
2.5 SPECIMEN CHARACTERIZATION .....	13
2.5.1 Phillips APD 3520 .....	13
2.5.2 FEI Tecnai F-20 Transmission Electron Microscope (TEM) .....	13
2.5.3 Cameca Local Electrode Atom Probe (LEAP®) 3000XSi.....	14
2.5.4 FEI Quanta Dual-Beam Focused Ion Beam (FIB).....	16
CHAPTER 3 MICROSTRUCTURE AND PHASE KINETICS.....	18

3.1 DIFFERENTIAL SCANNING CALORIMETRY (DSC) AND X-RAY DIFFRACTION (XRD) RESULTS.....	18
3.1.1 Differential Scanning Calorimetry (DSC) and X-ray diffraction (XRD) Discussion. .....	21
3.2 TRANSMISSION ELECTRON MICROSCOPY (TEM) AND ATOM PROBE TOMOGRAPHY (ATP) RESULTS.....	22
3.2.1 Transmission Electron Microscopy (TEM) and Atom Probe Tomography (ATP) Discussion.....	34
3.3 MAGNETIC MEASUREMENTS RESULTS .....	37
3.3.1 Magnetic Measurement Discussion .....	38
CHAPTER 4 CONCLUSION .....	39
4.1 MAJOR FINDINGS .....	39
4.2 FUTURE WORK.....	40
CHAPTER 5 REFERENCES.....	41
CHAPTER 6 APPENDIX .....	45

## LIST OF TABLES

<b>Table 3-1</b> The primary crystallization temperatures $T_p$ used for annealing of each ribbon with varying Ni content. * an exothermic peak for primary crystallization peak was not visible for this composition so this temperature was selected. ....	18
<b>Table 3-2:</b> Activation energies calculated from DSC data using Kissinger Method compared to Ni content (x). ....	21

## LIST OF FIGURES

<b>Figure 1-1</b> Coercivity plotted versus the grain size of various soft magnetic alloys.....	4
<b>Figure 2-1</b> Schematic of the melt-spinning process.....	9
<b>Figure 2-2</b> Portion of melt-spun ribbon from this alloy series.....	10
<b>Figure 2-3</b> Pictures illustrating each step in the lift-out procedure.....	16
<b>Figure 3-1</b> (a) DSC traces obtained from as-spun ribbons. (b) and (c) are XRD profiles of as-spun ribbons and annealed ribbons, respectively.....	20
<b>Figure 3-2</b> Selected area diffraction (SAD) patterns and bright field TEM images of as-spun $(Co_{1-X}Ni_X)_{88}Zr_7B_4Cu_1$ ( $X=0.25, 0.75$ and $1.00$ ) alloys. (a) and (b), (c) and (d) and (e) and (f) are those obtained from $(Co_{0.75}Ni_{0.25})_{88}Zr_7B_4Cu_1$ ( $X=0.25$ ), $(Co_{0.25}Ni_{0.75})_{88}Zr_7B_4Cu_1$ ( $X=0.75$ ) and $Co_{88}Zr_7B_4Cu_1$ ( $X=1.00$ ) alloy, respectively.....	23
<b>Figure 3-3</b> HAADF-STEM images obtained from as-spun (a) $(Co_{0.75}Ni_{0.25})_{88}Zr_7B_4Cu_1$ ( $X=0.25$ ) and (b) $Co_{88}Zr_7B_4Cu_1$ ( $X=1.00$ ) alloy. (c) is the dark field TEM image exciting a part of the Ni <sub>5</sub> Zr ring in Fig. 3-2 (e) obtained from $Co_{88}Zr_7B_4Cu_1$ ( $X=1.00$ ) alloy.....	24
<b>Figure 3-4</b> (a) Ion maps of Co, Ni, and B from the as-spun $(Co_{0.75}Ni_{0.25})_{88}Zr_7B_4Cu_1$ ( $X=0.25$ ) atom probe tip. (b) Proximity histogram generated from the Co isoconcentration surface (66.08 at.%) using voxel size of 2.1 nm. (c) 2D concentration map of Ni content with Cu cluster encircled.....	26
<b>Figure 3-5</b> (a) Ni isoconcentration surface (68.19 at.%) along with the B ions obtained from as-spun $(Co_{0.25}Ni_{0.75})_{88}Zr_7B_4Cu_1$ ( $X=0.75$ ) alloy. (b) Proximity histogram generated from the Ni isoconcentration surface (65.0 at.%) using a voxel size of 2.8nm. (c) 2D concentration map of Ni content with two different Cu clusters encircled. ....	28
<b>Figure 3-6</b> (a) Selected area diffraction (SAD) pattern and (b) bright field TEM images of the T <sub>p</sub> annealed $(Co_{0.75}Ni_{0.25})_{88}Zr_7B_4Cu_1$ ( $X=0.25$ ) alloy; and (c) Selected area diffraction (SAD) pattern and (d) bright field TEM images of the T <sub>p</sub> annealed $(Co_{0.25}Ni_{0.75})_{88}Zr_7B_4Cu_1$ ( $X=0.75$ ) alloy....	30

<b>Figure 3-7</b> (a) Ion maps of Co, Ni, and B from the annealed $(Co_{0.75}Ni_{0.25})_{88}Zr_7B_4Cu_1$ ( $X=0.25$ ) atom probe tip. (b) Proximity histogram generated from the Co isoconcentration surface (66.18 at.%) using a voxel size of 1.8 nm. (c) 2D concentration map of Co and Ni content respectively with same Cu clusters encircled. (d) 2D concentration map of Co and Ni content respectively with second different Cu clusters encircled than in part (c). .....	32
<b>Figure 3-8</b> (a) Ni isoconcentration surface (65.74 at.%) along with the B ions obtained from annealed $(Co_{0.25}Ni_{0.75})_{88}Zr_7B_4Cu_1$ ( $X=0.75$ ) alloy using a voxel size is 2.5 nm for the analysis of this dataset. (b) Proximity histogram generated from the Ni isoconcentration surface (65.74 at.%). (c) 2D concentration map of Ni content with Cu cluster. ....	33
<b>Figure 3-9</b> The nickel-cobalt binary phase diagram. ....	34
<b>Figure 3-10</b> (a) Saturation magnetization versus increasing Ni content ( $X$ ). (b) Coercivity versus increasing Ni content ( $X$ ).....	37
<b>Appendix 6-1</b> Weight conversions, final weights, and percent change for all compositions.....	46

## Chapter 1      Introduction

### 1.1    Soft Magnetic Materials

The main parameters in determining a material's usefulness as a soft magnet are coercivity, relative permeability, saturation magnetization, and electrical conductivity. Coercivity is the intensity of the magnetic field required to reduce the magnetization of a ferromagnetic material to zero after it has reached saturation. The intrinsic coercivity of soft magnetic materials is generally less than  $1000 \text{ Am}^{-1}$ . Relative permeability is a measure of how readily the material responds to the applied magnetic field. Saturation magnetization is the maximum remanent magnetization that a material can acquire after being placed in a direct magnetic field. Consequently, soft magnetic materials are classified as ferromagnetic and can be easily demagnetized by applying a reversing field. As a result, they have found use as power supply transformers where the material is continuously switched under an alternating current (AC) [1]. For direct current (DC) applications, these materials have found use as electromagnets, which can attract ferrous materials when a current is applied.

The materials being investigated in this work are for potential use in AC applications. Since these materials are primarily used in power supply transformers, research continues to look at ways to reduce the energy lost within the system. The energy loss occurs as the material is cycled through its hysteresis loop. There are three primary sources where energy loss originates in these magnetic based energy systems are hysteresis loss, eddy current loss, and anomalous loss [1]. For this study, the anomalous losses are of most interest because they deal with domain

wall motion as relates to crystallization kinetics. By understanding the crystallization behavior of these alloys, a better understanding between the crystalline and amorphous phase relationship and its affect on magnetic properties was explored.

## 1.2 Amorphous Materials

Amorphous magnetic ribbons peaked interest due to their excellent soft magnetic properties which is attributed to a lack of crystal anisotropy and grain boundaries. These attributes allow for application as transformer and inductive devices [1]. These amorphous materials have the general formula (3d-metal)<sub>80</sub>(metalloid)<sub>20</sub>, where 3d-metals = Fe, Co, Ni and metalloid = B, Si, C, etc [2]. The metalloid's role is to lower the melting point of the alloy, which helps in stabilizing the amorphous phase [2]. The intrinsic, magnetic properties of Fe and Co consequently resulted in Fe-Co-based amorphous alloys being the most promising systems [2].

The production of amorphous materials can be accomplished one of two ways. Either by a melt-spinning technique that produces thin ribbons (thickness 20-50  $\mu\text{m}$ ) [3,4] or by an in-water-quenching techniques that produces wires (thickness 80-120  $\mu\text{m}$ ) [5]. During this quenching process, two unwanted anisotropies develop. The first is stress-induced anisotropies and, second is shape anisotropy due to surface roughness [2]. These two anisotropies cause the demagnetizing field of the material not to be equal for all directions, creating one or more magnetic/ easy axis. This uneven demagnetizing field is detrimental to an amorphous material's soft magnetic properties specifically its permeability. The effect of decreasing the permeability is an increase in core losses thus eliminating the material as a practical system for transformer applications [6].

### 1.3 Nanocrystalline Soft Magnetic Materials

#### 1.3.1 Nanocrystalline Soft Magnetic Materials

To overcome these magnetic property concerns with amorphous alloys, the precipitation of nanocrystallites within the amorphous matrix has been proposed. The nanocrystallites formation occurs by annealing amorphous ribbons at an optimum temperature and over an optimum annealing time where nucleation and growth occur to precipitate out these crystallites [2]. A consequence of this microstructure is an exchange coupling between nanocrystallites by means of the magnetic amorphous phase, this yields nanocrystalline materials with excellent soft magnetic properties meaning materials that possess both low coercivity and high permeability [2]. Herzer showed the softening of the magnetic properties is due to the grain size being smaller than the magnetic exchange length, which causes an averaging of the magnetic anisotropy of the nanocrystallites [7]. This results in a low value of the effective anisotropy [7,8]. On a macroscopic level, coercivity is reduced considerably and permeability is increased by this exchange coupling [2]. The reduction of coercivity,  $H_c$ , in nanocrystallites scales as  $D^6$  [7]. Similarly the permeability,  $\mu_i$ , increases with decreasing grain size [7].

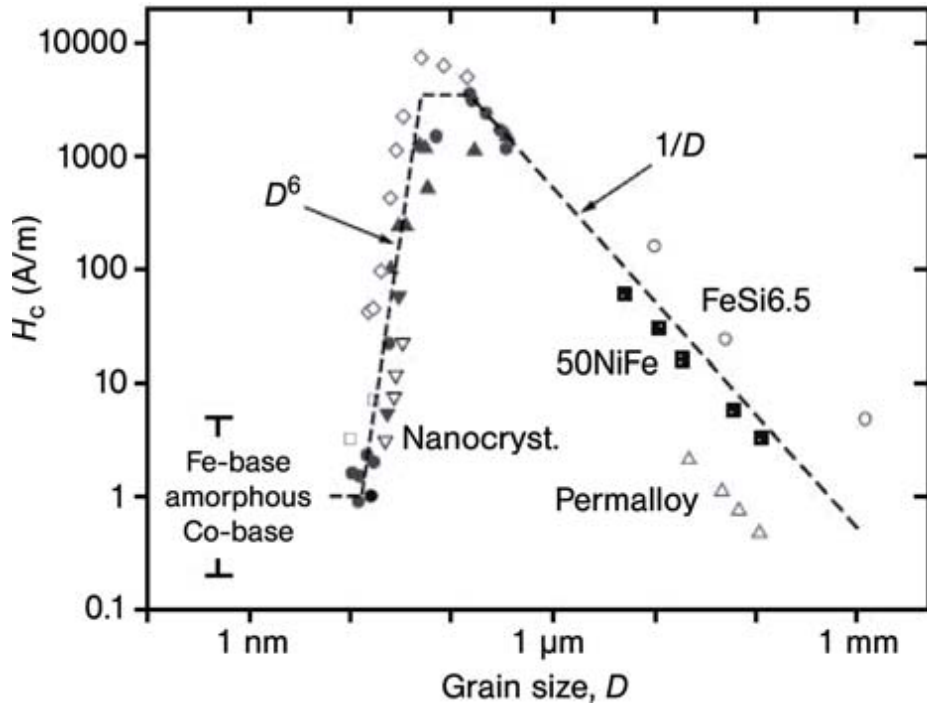


**Figure 1-1** Coercivity plotted versus the grain size of various soft magnetic alloys.

A plot of coercivity as a function of grain size for various soft magnetic alloys is shown in Figure 1-1 [7,9]. The lines with the slopes of  $D^6$  and  $D^{-1}$  represent the two switching mechanisms: exchange averaged anisotropy and domain wall pinning, respectively [10]. The least desirable soft magnetic performance results at the point of intersection of these two switching mechanisms and is known as the exchange correlation length (roughly the width of the magnetic domain wall) [10]. The  $D^{-1}$  line corresponds to conventional crystalline alloys which clearly improve with increasing grain size because of lesser amounts of domain wall pinning at grain boundaries [10]. The  $D^6$  line corresponds to amorphous alloys, with their lack of grains and grain boundaries, results in lower losses than the conventional large-grained alloys [10].

### 1.3.2 FINEMET / VITROPERM

In 1988 Yoshizawa *et al.* produced the first of these nanocrystalline commercial materials,  $\text{Fe}_{73.5}\text{Cu}_1\text{Nb}_3\text{Si}_{13.5}\text{B}_9$ , by altering a common Fe-Si-B amorphous alloy with the addition of small amounts of Nb and Cu [11,12]. This alloy type is referred to as either FINEMET or VITROPERM [2]. The addition of Cu and Nb acted as nucleation sites for  $\alpha$ -(Fe,Si) nanocrystallites and hindered grain growth yielding crystals with grain sizes of about 10-20 nm [11]. The alloys based on the Fe-Si-Nb-B-Cu composition have extremely low losses with moderate saturation magnetization and operation temperatures [7, 13]. This alloy type can be operated effectively up to about 120°C without degradation of performance because of the Curie temperature of amorphous phase,  $T_c^{\text{am}}$ , being close to 327°C (~600K) [10]. From this initial composition other nanocrystalline material were created by slight alteration to this original nanocrystalline composition.

### 1.3.3 NANOPERM

The NANOPERM-type alloys with the general composition of Fe-Zr-B-(Cu) are most closely related to the FINEMET alloys. This composition yields  $\alpha$ -Fe nanocrystallites, which has the advantage of 20% larger magnetization over FINEMET's  $\alpha$ -(Fe,Si) nanocrystallite [14]. However the  $\alpha$ -Fe based NANOPERM has a lower operation temperature and slightly larger losses than the  $\alpha$ -(Fe,Si) based FINEMET-type alloys. This lower operation temperature limits their use to room temperature application because of their lower  $T_c^{\text{am}}$ . In addition, the production of this alloy is more difficult because of the highly reactive nature of Zr forming oxides which further deteriorate the magnetic properties [2].

### 1.3.4 HITPERM

From the NANOPERM alloy type, another alloy type, HITPERM, evolved by the simply addition of another element, Co, and has the general formula of Fe-Co-Zr-B-(Cu). This

nanocrystalline material is based on the formation of  $\alpha$ - and  $\alpha'$ -(Fe,Co) crystallites [10]. These  $\alpha$ - and  $\alpha'$ -(Fe,Co) crystallites, with their A2 and B2 crystal structures respectively, result in high permeability and potential higher operation temperature for the alloy system [15]. The potential higher operation temperature can exceed 600°C as the substitution of Co and Fe approaches 50% because of the significant improvement in  $T_c^{am}$  [16-18].

### 1.3.5 Microstructure Engineering Magnetic Nanocrystalline and Amorphous Alloys

From these three common alloys systems a general chemical equation for all nanocrystalline alloys can be seen to be (Fe,Co,Ni)-M-(B,Si)-Cu. The first series of elements (Fe, Co, Ni) are ferromagnetic transition metals and compose the majority weight fraction of the alloy. These elements provide large magnetization and a high Curie temperature [10]. The M element represents early transition metals in the periodic table (such as Zr, Hf, and Mo) and is believed to help to impede growth by increasing activation energies for diffusion with regard to Fe-based metallic glasses [19]. The B and Si additions stabilize the amorphous matrix phase [19]. Arguably, the Fe-Co-Zr-B-(Cu) alloys with  $\alpha$ - and  $\alpha'$ -(Fe,Co) crystallites, referred to as HITPERM-type alloys, are the most mature in terms of microstructural engineering and magnetic property performances.

In the current work, this research has branched out from HITPERM by exploring crystalline kinetics, microstructure formations and magnetic properties in the Ni:Co ratio rather than the Fe:Co ratio. The Ni-based alloys have lower magnetization saturation than the Fe alloys making those less likely candidates for magnetic energy based applications. However, Ni-based alloys have faster crystallization kinetics than Fe-based alloys, while Co-based alloys have the slowest kinetics of these three [20]. Thus by selecting Ni:Co based alloy this research will

provide the last data needed to cover the complete range from the fastest to the slowest crystallization kinetics with regard to these elements.

Finally, there have been multiple studies investigating whether Cu clusters act as heterogeneous nucleation sites for microstructural engineering these crystallites [21-23]. In one study it was indicated that the addition of Cu provides heterogeneous nucleation sites for the nanocrystallites  $\alpha$ -FeCo in the HITPERM Fe-Co-Nb-B alloys [21]. Another study reported Cu clusters do not form in HITPERM alloys containing Zr, making it impossible for Cu to act as heterogeneous nucleation sites [22]. A final study indicated as Co content increased in FINEMET alloys, a decrease in the number density of Cu clusters occurred thus reducing their ability to be heterogeneous nucleation sites [23]. As a result of the different kinetics possessed by this system, the role Cu plays in this alloy system will also be investigated to determine whether or not Cu clusters, and if it does whether or not it acts as heterogeneous nucleation sites for crystallization to determine its correlation to the varying results in the current literature. If the Cu or Cu clusters play no role as a heterogeneous nucleation site, it can be removed for the alloy system since it provides no benefit as a nucleation site or as a magnetic material itself.

While this Ni:Co alloy system will not optimize the soft magnetic properties, it will provide critical data with regard to crystallization kinetics for the nanocrystalline research community. This data will only lead to improvements in the microstructural engineering of nanocrystalline material, which is the most crucial factor for all these aforementioned material systems.

## Chapter 2      Experimental

### 2.1    Melt-Spinning Processing

Amorphous metals are a subdivision of bulk metals. The unique feature differentiating amorphous metals from bulk metals is their disordered atomic structure. This disordered structure is the basis for amorphous metals being categorized as non-crystalline, while most metals with their highly ordered atomic arrangements are categorized as crystalline materials. Amorphous metals generally achieve this disordered atomic structure through an extremely rapid cooling process of the liquid metal, but other techniques including physical vapor deposition, solid-state reactions, ion irradiation, and mechanical alloying can produce amorphous metals [10, 24-27]. One example of an extremely rapid cooling procedure is melt-spinning, which was utilized to producing the alloys in this research. Melt-spinning generates rapid cooling on the order of  $10^6$  °C/sec by pouring molten metal onto a spinning metal disk. This rapid cooling is so fast that crystallization does not occur and a glassy metal or amorphous phase results.

A series of  $(Co_{1-x}Ni_x)_{88}Zr_7B_4Cu_1$  alloys with different Ni content ( $x = 0, 0.25, 0.5, 0.75, 1$ ) were studied. Five ingots at the designated compositions were made via arc melting under an Ar atmosphere with a Ti getter to further reduce any possible oxidation. Each elemental constituents were > 99.97 at.% pure. The elemental constituents for each composition were weighed together to get an overall weight for the composition. The ingots were remelted at least three times to ensure all elemental constituents were homogeneously melted within the ingot. Once the ingots had cooled to room temperature, they were weighed and the percent

weight change was calculated to ensure that any change was  $< 1\%$ . Weight changes greater than that would suggest oxidation or crucible contaminants in the sample creating weight gains or losses. The weight conversions, final weights, and percent change for all the compositions can be seen in Appendix 6-1. The last step in prepping the ingots was to remove their outer layer to ensure no oxides remained by manually grinding this layer off.

The ingot was then prepared for the melt-spinning process. This was done by placing a Boron Nitride tube in a lathe and rotating it. While the tube was rotating, an oxygen torch was placed on one end of the tube. The heat from the torch caused the end of the tube to enclose upon itself. Once an orifice was  $\approx 24$ - $32$  mils at the end of the tube, the heat was removed.

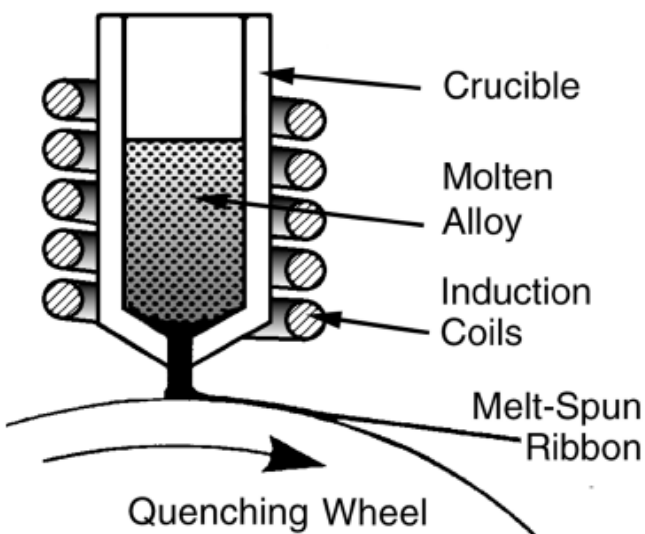


**Figure 2-1** Schematic of the melt-spinning process.

A schematic of the entire melt-spinning process can be seen in Figure 2-1. For the melt-spinning process, the ingot was placed within the Boron Nitride tube which acts as the crucible, while the open end of the tube had cork placed in it. Through the cork, a gas line of He was run.

The crucible was placed within the high frequency coils where the crucible is positioned during the melt-spinning process. Once the cork and crucible were secured into place, the melt-spinning apparatus door was closed, and a mechanical pump was used to evacuate the chamber before the process begins. Then the Cu wheel speed was gradually turned up to 50 m/s, and the current running through the coils was increased until the ingot liquefied because of induction heating. A partial pressure of He was then applied to the liquefied ingot to overcome the surface tension of the liquid forcing its ejection onto the rapidly spinning Cu wheel. The molten material, once in contact with the spinning Cu wheel, solidified at cooling rates of up to  $10^6$  °C/s [10]. The rapid cooling promoted amorphous structure upon cooling. The re-solidified alloy formed into ribbons that were approximately 20-60  $\mu\text{m}$  in thickness and 2-3 mm in width, respectively. A portion of one of the ribbons can be seen in Figure 2-2. The entire ingot was ejected on the rotating Cu wheel in approximately 5-10 seconds.



**Figure 2-2** Portion of melt-spun ribbon from this alloy series.

## 2.2 Differential Scanning Calorimetry (DSC)

The ribbons were analyzed by Differential Scanning Calorimetry (DSC) to determine the primary and secondary crystallization temperatures of the ribbons. The DSC was performed using a Netzsch STA 449 F1 Jupiter system at scanning rates of 2, 5, 10, 20, and 50°C/min. DSC works by having a reference system and the sample to be analyzed in a chamber that was cycled through a range of temperatures. The machine measured the difference in temperature between the sample and a Pt cup reference, which does not undergo any phase transformation event. Thus, any temperature difference recorded indicates either an exothermic or endothermic event occurring within the sample. The crystallization was an exothermic event within these samples. For this experiment, approximately 10 grams of the varying compositions were placed into a Pt cup with the reference cup remaining empty. The heating cycle went from 25°C to 925°C for all the runs for these compositions.

From the DSC runs, the primary and secondary crystallization temperatures for each alloy were determined. With this knowledge, the Kissinger Method was used to calculate the activation energy, Q (kJ/mol), for primary crystallization at each composition [28]. The Kissinger equation is generally written as

$$-\ln\left(\frac{\Phi}{T_p^2}\right) = -\ln\left(\frac{AR}{Q}\right) + \left(\frac{1}{T_p}\right)\left(\frac{Q}{R}\right) \quad 2.1$$

where  $\Phi$ ,  $T_p$ , A, R, and Q represent the heating rate, primary crystallization temperature, a pre-exponential factor, the gas constant, and activation energy respectively. The Kissinger Method works by plotting the inverse of the primary crystallization temperature in Kelvin (K) versus the natural logarithm of the heating rate divided by the primary crystallization temperature squared.

The slope of these lines multiplied by the universal gas constant (R) yields the activation energy (Q) for crystallization.

### 2.3 Encapsulations and Heat Treatment

From the primary and secondary crystallization determined using DSC, one annealing temperatures for each composition was set. The temperature selected for each composition was the primary crystallization peak temperature ( $T_p$ ). All of these anneals were performed in a box furnace for one hour and water quenched when finished. All of the samples used for annealing were encapsulated in Boron Nitride tubing. In the similar fashion as was used to preparing the crucible, the tube was placed in a lathe and rotated. While the tube was rotated, an oxygen torch was placed on one end of the tube with the heat causing the end of the tube to enclose upon itself.

Once the end of the sealed tube had cooled to room temperature, a sample was placed in the enclosed end. Then a neck was created in the tubing above the sample by placing the torch on this section and using the lathe to slowly stretch the tube to a thinner diameter while it was malleable from the heat. After the neck had cooled, a Ti getter was placed above the neck. A final neck was created on the other side of the Ti getter. The tube was removed from the lathe and the open end of the tube was placed into a fixture with a mechanical pump attached. A vacuum was pulled on the tube and then backfilled with argon. This step was repeated three times to remove all residual oxygen. After the last backfill of argon, the torch was used to completely seal the last neck created above the Ti getter.

## 2.4 Magnetic Properties Measurement

The ribbons were analyzed by Vibrating Sample Magnetometry (VSM) to determine the coercivity and saturation magnetization for each ribbon. The VSM was performed using a DMS VSM Model 4HF. The coercivity measurements were performed at room temperature using an applied, reversible field of 20 kOe.

## 2.5 Specimen Characterization

The following instruments and techniques were used to characterize the processed specimens. Detailed procedures are given in the proceeding sections. The results and calculations incorporated with them may be found in the following chapter and appendix.

### 2.5.1 Phillips APD 3520

The first technique used for phase identification was X-ray diffraction (XRD). The actual scans were performed with a Phillips APD 3520 using a Cu K<sub>α</sub> source. The parameters used for each scan were a step interval of 0.02 degrees/step and a collection time of 2 seconds/step. In addition, all scans were performed on the wheel side of the ribbons. The ribbons were cut into lengths of approximately 12-15 cm with five to seven lengths of ribbon taped side by side onto the glass slide using adhesive carbon tape.

### 2.5.2 FEI Tecnai F-20 Transmission Electron Microscope (TEM)

The microstructure characterization was performed using a 200 keV field emission FEI F20 G<sup>2</sup> F20 Supertwin (scanning) transmission electron microscope ((S)TEM). Bright and dark field imaging was used to differentiate between the crystalline and amorphous regions within the specimen and calculate average grain size for the different specimens. Selected Area Electron Diffraction (SAED) allowed for indexing of diffraction patterns to identify crystalline phases

present within the specimen. Finally, High Angle Annular Dark Field (HAADF) images were taken to provide qualitative compositional information. In the HAADF mode, the intensity scales with atomic number,  $\sim Z^{1.7-2}$  [29] with higher-atomic number species appearing brighter.

TEM specimens were prepared by ultrasonically drilling 3 mm diameter discs from the ribbon material. The next step varied slightly depending on the sample's thickness. If the thickness was  $< 25 \mu\text{m}$ , the sample was immediately ion-milled. If the thickness was  $> 25 \mu\text{m}$ , the sample was dimpled in the middle of the discs with 6 micron diamond past and then ion-milled. The ion-milling was performed using the Precision Ion Polishing System (GATAN691) at 4 keV, 24-30 mA, and top and bottom incident angle of 10° to create the initial perforation. The perforation's edges were then "cleaned up" using 1-2 keV, 8-20 mA, and top and bottom angles of 7° for final thinning. For the samples that indicated the presence of any amorphous phase, the ion-milling was performed at cryogenic temperature using a liquid nitrogen cold finger at the specimen foil. This ensured the sample did not heat-up and generate an artificial crystallization from the sample preparation.

### 2.5.3 Cameca Local Electrode Atom Probe (LEAP®) 3000XS

Atom probe tomography (APT), which provides a three dimensional reconstructed rendering of atoms with near atomic resolution, was utilized to further investigate the spatial compositions in these alloys. The technique works by applying a high voltage pulse to a specimen tip that has a radius of curvature of  $\sim 50$ - $100 \text{ nm}$  whereupon atoms on the surface field evaporate [30-32]. The atoms, now ions, are accelerated to a position sensitive and time-of-flight detector used to determine the spatial location of the individual atoms (through reconstructing the flight paths) with near atomic 3-dimensional resolution ( $z < 0.05 \text{ nm}$  and  $x-y < 0.5 \text{ nm}$ ). The atoms are identified by their mass-to-charge ratio. Recent advances over the past

decade have allowed the atom probe technique to expand the field of view from ~ 15 nm to over 200 nm [33], easily assuring the region of interest can be captured. The positively charged, mass spectral time-of-flight detector collects the ionized atoms from the specimen of interest due to the field applied to it [30,34]. By reconstructing the evaporated ions' path, a three-dimensional model of the ions positions can be generated which can then provide local chemistry around the ion. The time-of-flight detector works by pulsing either an applied voltage in voltage mode or a laser in laser mode then measuring the time for the ion to hit the detector to determine the mass over charge ratio ( $m/q$ ) of the ion.

The APT analysis was performed using a Cameca (formally Imago Scientific Instruments) Local Electrode Atom Probe (LEAP®) 3000XSi. The LEAP has higher data acquisition rates and an increased field of views (>100nm) in comparison to traditional atom probes [32]. The LEAP analysis chamber was maintained  $< 10^{-10}$  Torr. The atom probe analysis of the as-spun  $(Co_{0.75}Ni_{0.25})_{88}Zr_7B_4Cu_1$  ( $X=0.25$ ) was ran in laser mode at a base set-point temperature of 30 K, a pulse energy of 0.2 nJ, and a pulse rate of 250 kHz because of a propensity of fracture failures noted when the sample was field evaporated in the voltage evaporation mode. The pulsing electric field can generate significant electrical-induced stress in the tip. The atom probe analyses for all other specimens were run in the voltage mode with a base set-point temperature of 30 K, pulse fraction of 20 - 25%, and a pulse rate of 200 kHz. The obtained LEAP datasets were analyzed using Imago's Visualization and Analysis Software (IVAS) 3.4.1.

To ensure accurate data analysis, optimization of voxel size was performed which (1) showed the phase composition consistent with nominal composition, and (2) minimized the value of the length of compositional profile,  $\Delta C_f$ . Note that the length of compositional profile,

$\Delta C_f$  is a parameter for selection of block size defined by the length of the composition profile [35]. For further details on optimization of voxel size read [36].

#### 2.5.4 FEI Quanta Dual-Beam Focused Ion Beam (FIB)

For a sample to be field evaporated in the LEAP, a specimen must have a radii of curvature of ~100 nm or smaller. To achieve a needle like geometry, the atom probe specimens were prepared via site-specific extraction using a FEI Quanta Dual-Beam focused ion beam – scanning electron microscope (FIB-SEM), which was equipped with an Omniprobe micromanipulation lift-out system and a gas injection system (GIS). In the atom probe specimen preparation, a sacrificial Pt cap was deposited onto the specimen surface to reduce Ga ion damage and implantation [37]. In addition, the initial cutting was performed using an accelerating voltage of 30 keV in the FIB with the final milling utilized an accelerating voltage of 5 keV, which dramatically reduced the Ga ion implantation and surface damage to the specimen [38]. The lift-out specimens were placed onto pre-fabricated Si mounting posts and attached to the post using the Gas Injection System (GIS) Pt deposition tool of the FIB. This step and the step's prior can be seen in Figure 2.3.

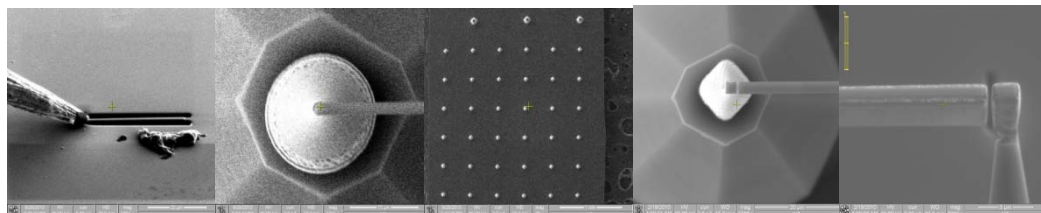


**Figure 2-3** Pictures illustrating each step in the lift-out procedure.

After the individual specimens were attached to the Si posts, annular ion milling was used to sharpen the tips to the appropriate geometric needle shape required for field evaporation. During this sharpening process typically large diameters and higher beam currents were utilized

first and sequentially decreased as one proceeds through the multiple annular FIB milling steps [37]. Further details of FIB-based atom probe preparation can be found elsewhere [39].

## Chapter 3 Microstructure and Phase Kinetics

### 3.1 Differential Scanning Calorimetry (DSC) and X-ray diffraction (XRD) Results

The primary crystallization temperatures,  $T_p$ , for each of the compositions were determined by Differential Scanning Calorimetry (DSC). Figure 3-1(a) shows the exothermic peak associated with the  $T_p$  for each of the as-spun ribbons. The  $T_p$  temperatures are tabulated in Table 3-1. A  $T_p$  was noted for all specimen except the X=1.0 or the Co-free ribbon. As the Ni content increased, the exothermic heat flow shifted to a lower temperature and its intensity decreased. These results indicated a pre-existing volume fraction of crystalline phase prior to annealing and would be consistent with the structural characterization results above. The lack of a  $T_p$  in the X=1.0 ribbon suggested that the ribbon was fully or nearly fully crystallized in the as-spun state. Based on these DSC results, the following three annealing temperatures were chosen for each specimen: 20°C below  $T_p$ ,  $T_p$ , and 50°C above  $T_p$  for one hour.

**Table 3-1** The primary crystallization temperatures  $T_p$  used for annealing of each ribbon with varying Ni content. \* an exothermic peak for primary crystallization peak was not visible for this composition so this temperature was selected.

(Co <sub>1-x</sub> Ni <sub>x</sub> ) <sub>88</sub> Zr <sub>7</sub> B <sub>4</sub> Cu <sub>1</sub> ; Nickel Content (X)	$T_p$ annealing temperatures (°C)
1.0	424°C *
0.75	411°C
0.5	415°C
0.25	447°C
0	490°C

For the Co-rich and equi-atomic ribbons ( $X=0$ ,  $0.25$ , and  $0.5$ ), the XRD spectrum for the as-spun alloys, Figure 3-1(b), showed broad peaks near  $45$  degrees and  $80$  degrees  $2\Theta$ . This is indicative of an amorphous structure, which was confirmed by the TEM micrographs shown in Figure 3-2. As the Ni content increased ( $X=0.75$  and  $1.0$ ) the clear onset of crystallization was evident in the XRD spectrum seen in Figure 3-1(b). The broad peaks in the high angle spectrum were replaced with sharp peaks. These peaks were consistently indexed to a face centered cubic (fcc) phase. The onset of these prevalent diffracted peaks is indicative of partial or full crystallization in the microstructure. The presence of more crystalline phase would explain the decrease in the DSC crystalline peak since a portion of the sample was already crystallized in the as-spun state. The XRD spectrums of the alloys annealed at  $T_p$  are plotted in Figure 3-1(c). A transition from a hexagonal close packed (hcp) main crystalline phase for the Co-rich ribbons ( $X \leq 0.5$ ) to a primary face-centered cubic (fcc) phase is observed with increasing Ni content. At  $X=1.0$ , an additional crystalline phase,  $\text{Ni}_5\text{Zr}$ , was observed. Additional diffraction rings of  $\text{Ni}_5\text{Zr}$  were observed in the electron diffraction results to be shown in Chapter 3.1.

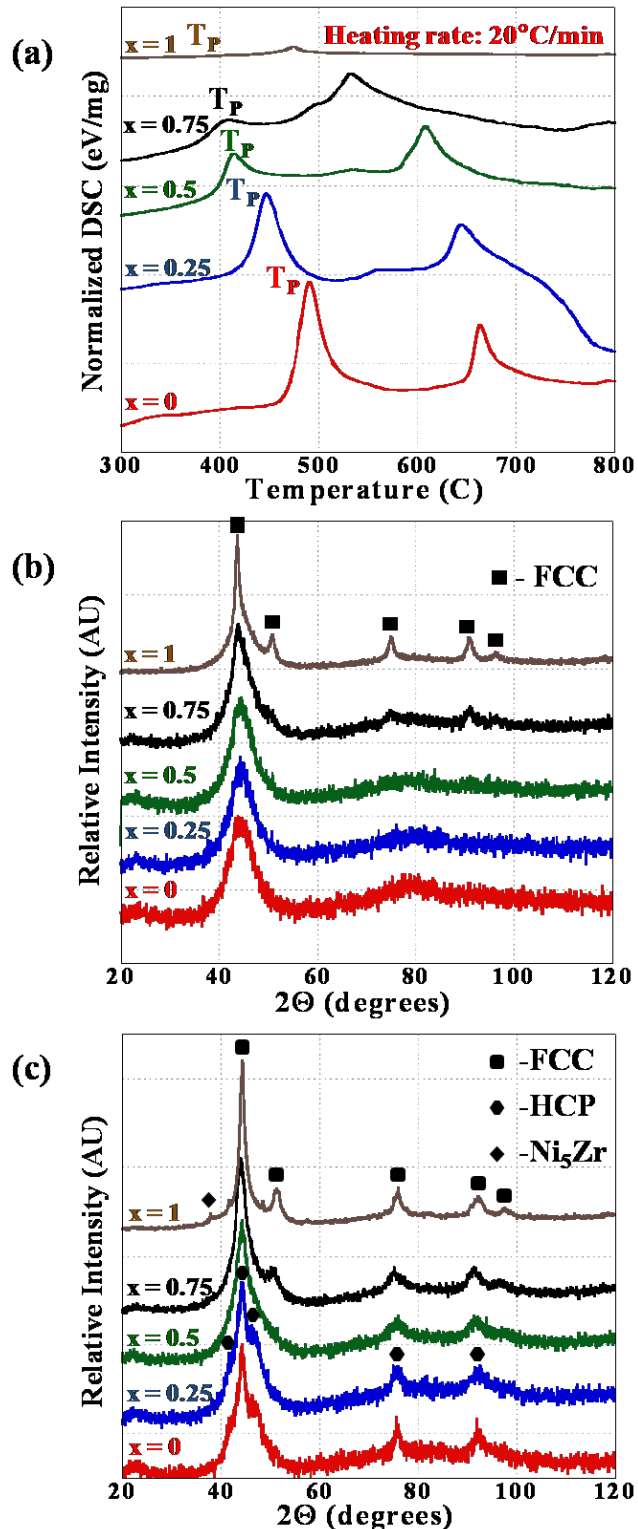


**Figure 3-1** (a) DSC traces obtained from as-spun ribbons. (b) and (c) are XRD profiles of as-spun ribbons and annealed ribbons, respectively.

### 3.1.1 Differential Scanning Calorimetry (DSC) and X-ray diffraction (XRD) Discussion

With increasing Ni content, the  $(Co_{1-x}Ni_x)_{88}Zr_7B_4Cu_1$  alloys exhibited faster crystallization kinetics. This was manifested by the presence of the crystalline phases, even in the as-spun condition, for the X=0.75 and 1.0 ribbons' XRD spectra, TEM characterization, and lower T<sub>p</sub> peak's in the DSC curves. Using the Kissinger method [28], the activation energies were determined using the DSC data of Figure 3-1(a). Table 3-2 is a tabulation of the results which confirmed a decreasing activation energy barrier with increasing Ni content. Clearly, this reduction plays a dominate role in the crystallization of alloy.

**Table 3-2:** Activation energies calculated from DSC data using Kissinger Method compared to Ni content (x).

$(Co_{1-x}Ni_x)_{88}Zr_7B_4Cu_1$ Nickel Content (X)	Activation Energy (kJ/mol)
0	322
0.25	284
0.5	225
0.75	201

### 3.2 Transmission Electron Microscopy (TEM) and Atom Probe Tomography (APT) Results

TEM micrographs, Figure 3- 2, of as-spun  $(Co_{1-x}Ni_x)_{88}Zr_7B_4Cu_1$  ( $X=0.25, 0.75$  and  $1.00$ ) alloys were taken. For the  $(Co_{0.75}Ni_{0.25})_{88}Zr_7B_4Cu_1$  ( $X=0.25$ ) alloy, the selected area diffraction (SAED) patterns and the bright field TEM micrographs in Figures 3-2(a) and (b), respectively, confirmed that the majority of the alloy consisted of an amorphous phase. Upon closer inspection of the SAED pattern, Figure 3-2(a), a faint hexagonal close packed (hcp) ring can be indexed. These nanoscale crystallites are evident by their diffraction contrast in Figure 3-2(b). The lack of XRD diffraction of this phase confirms that its volume fraction was below the XRD detection limit. This is in agreement with these TEM results which showed that the crystallites are rare and spatially well separated. The TEM SAED and bright field images of the Ni-rich ( $X=0.75$  and  $1.0$ ) ribbons, Figures 3-2(c)-(f), clearly revealed crystalline diffraction rings, whose phase is consistent with the XRD pattern. The diffraction contrast from the crystallites is apparent in Figure 3-2(d) and (f)'s micrographs. Upon reviewing the bright field micrographs for the  $X=0.25, 0.75$  and  $1.0$  ribbons, the crystallites consistently increased in size from approximately  $5$  nm up to  $50$  nm with increasing Ni-content.

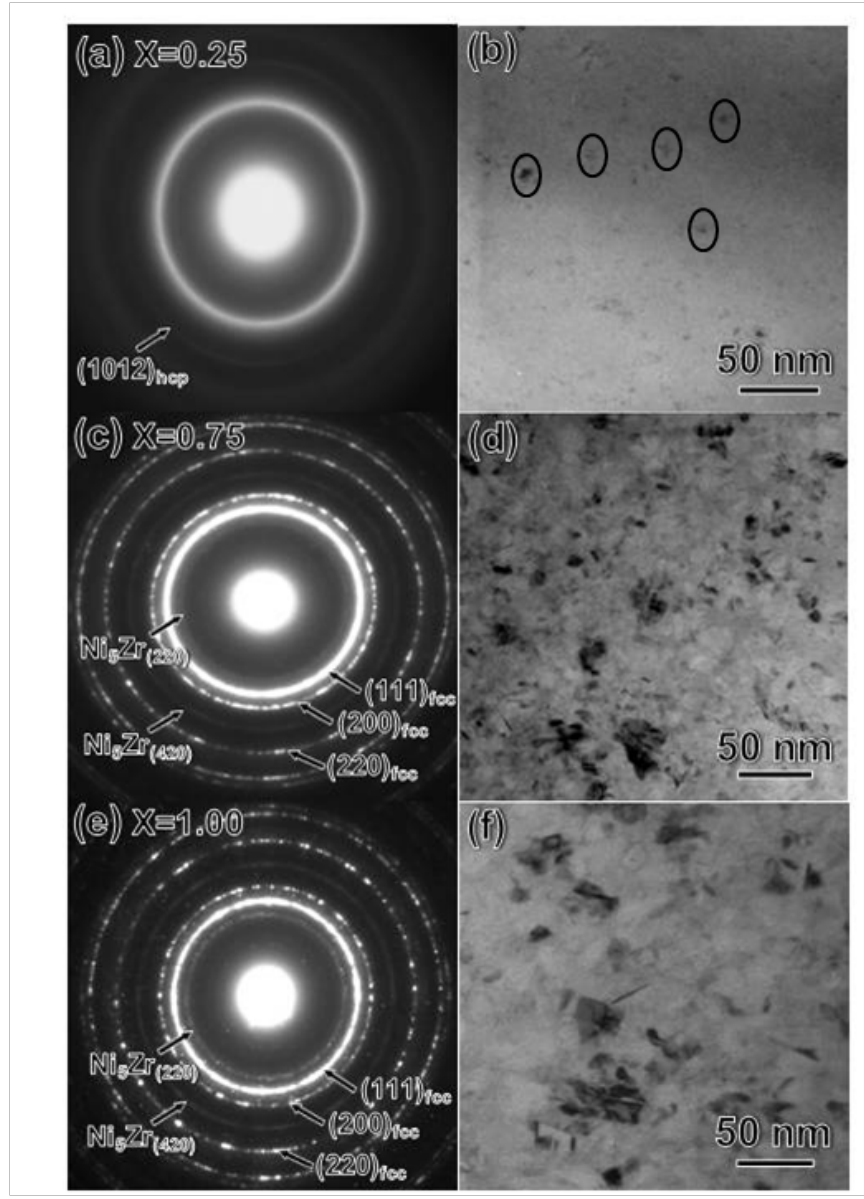


**Figure 3-2** Selected area diffraction (SAD) patterns and bright field TEM images of as-spun  $(\text{Co}_{1-\text{x}}\text{Ni}_\text{x})_{88}\text{Zr}_7\text{B}_4\text{Cu}_1$  ( $\text{x}=0.25, 0.75$  and  $1.00$ ) alloys. (a) and (b), (c) and (d) and (e) and (f) are those obtained from  $(\text{Co}_{0.75}\text{Ni}_{0.25})_{88}\text{Zr}_7\text{B}_4\text{Cu}_1$  ( $\text{x}=0.25$ ) ,  $(\text{Co}_{0.25}\text{Ni}_{0.75})_{88}\text{Zr}_7\text{B}_4\text{Cu}_1$  ( $\text{x}=0.75$ ) and  $\text{Co}_{88}\text{Zr}_7\text{B}_4\text{Cu}_1$  ( $\text{x}=1.00$ ) alloy, respectively.

High Angle Annular Dark Field (HAADF)-Scanning TEM (STEM) images of the as-spun  $(Co_{0.75}Ni_{0.25})_{88}Zr_7B_4Cu_1$  ( $X=0.25$ ) and  $(Co_{0.25}Ni_{0.75})_{88}Zr_7B_4Cu_1$  ( $X=0.75$ ) alloys, Figure 3-3 (a) and (b), were taken to provide qualitative compositional information. Recall that the higher atomic number species appear brighter in HAADF images. In both images, the grain boundaries are observed to exhibit a dimmer contrast than the interior portion of the grains. This indicates possible chemical partitioning of the low atomic species to the grain boundaries. As will be shown in the atom probe data, boron was found to be preferentially enriched in the grain boundaries. A dark field image, Figure 3-3(c), also revealed fine Ni-rich particles in the grain boundaries using the  $Ni_5Zr$  rings in Figure 3-2 (c).

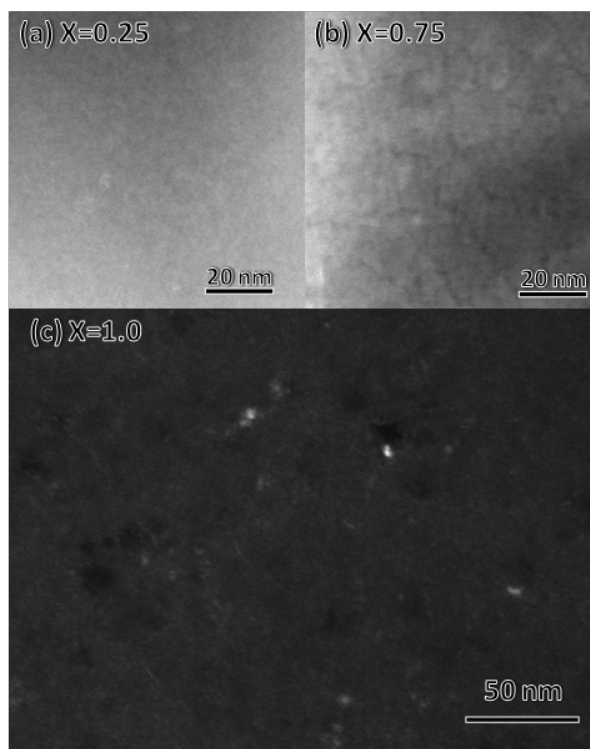


**Figure 3-3** HAADF-STEM images obtained from as-spun (a)  $(Co_{0.75}Ni_{0.25})_{88}Zr_7B_4Cu_1$  ( $X=0.25$ ) and (b)  $Co_{88}Zr_7B_4Cu_1$  ( $X=1.00$ ) alloy. (c) is the dark field TEM image exciting a part of the  $Ni_5Zr$  ring in Fig. 3-2 (e) obtained from  $Co_{88}Zr_7B_4Cu_1$  ( $X=1.00$ ) alloy.

Atom probe tomography reconstructions, Figure 3-4(a-c), of the  $(Co_{0.75}Ni_{0.25})_{88}Zr_7B_4Cu_1$  ( $X=0.25$ ) ribbon revealed chemical partitioning and clustering in the as-spun state. An enrichment of Co is detected to be in the amorphous phase where as the Ni partitioned to the crystalline phase, Figure 3-4(b). A slight increase in Zr is also noted in the Ni crystalline phase as compared to the Co amorphous phase. With regards to B and Cu, there appears to be no preferential segregation to the Co-rich amorphous phase or the Ni-rich crystalline phase. A clustering analysis, that utilized the envelope clustering method [40], was performed to determine if Cu was acting as a heterogeneous nucleation site for the Ni-rich crystallites. If the clusters are enveloped by the Ni content, one could infer that it acted as a heterogenous nucleation site. From the concentration map in Figure 3-4(c), the Cu cluster is in a region with neither the highest nor the lowest Ni content. This suggests the Cu is not acting as a heterogeneous nucleation site for crystallization.

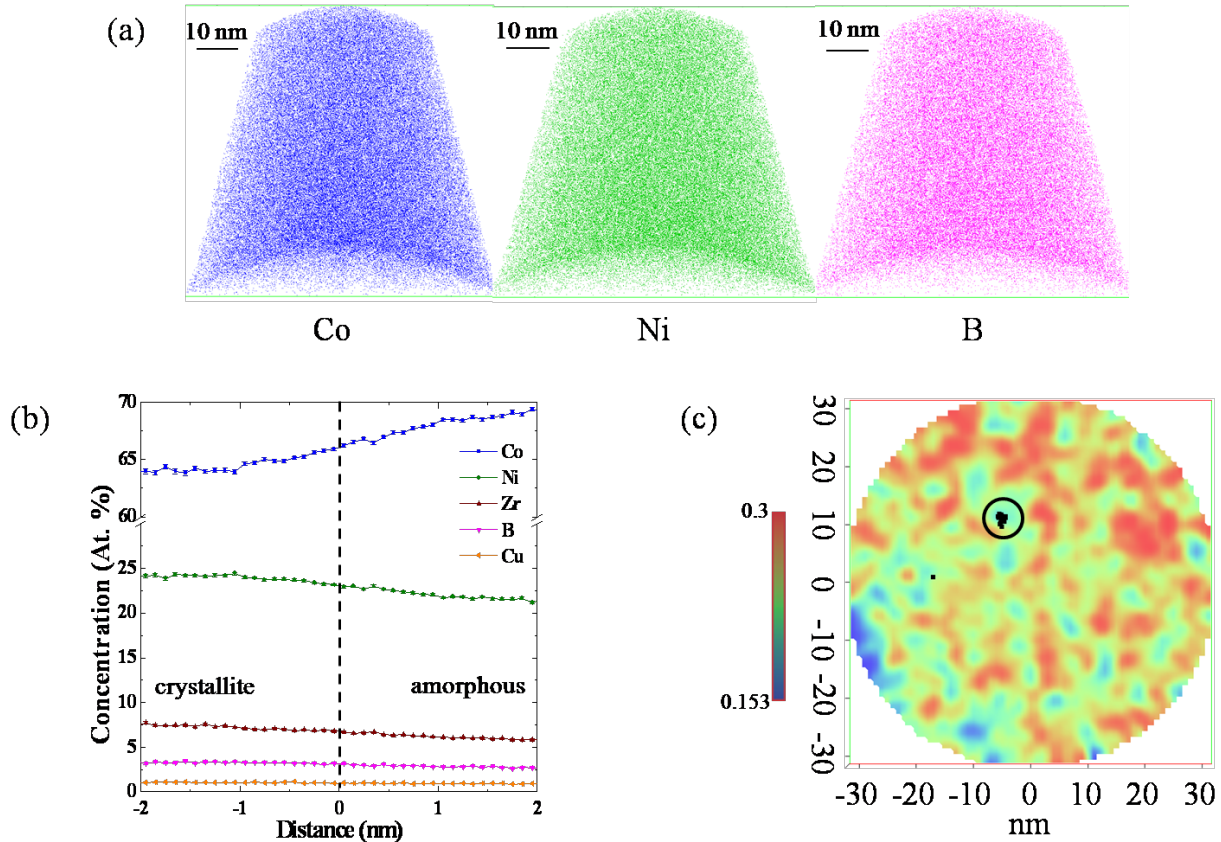


**Figure 3-4** (a) Ion maps of Co, Ni, and B from the as-spun  $(\text{Co}_{0.75}\text{Ni}_{0.25})_{88}\text{Zr}_7\text{B}_4\text{Cu}_1$  ( $X=0.25$ ) atom probe tip. (b) Proximity histogram generated from the Co isoconcentration surface (66.08 at. %) using voxel size of 2.1 nm. (c) 2D concentration map of Ni content with Cu cluster encircled.

Atom probe tomography reconstructions, Figure 3-5(a-c), were conducted on the  $(Co_{0.25}Ni_{0.75})_{88}Zr_7B_4Cu_1$  ( $X=0.75$ ) ribbon. The proximity histogram, Figure 3-5(b), confirmed a partitioning of Ni to the crystalline phase and a strong depletion of Co away from the crystalline phase. As noted previously in Figure 3-4, there appeared to be a slight increase in Zr concentration in the crystalline phase as compared to the intergranular matrix. A clustering analysis was once again performed to determine if Cu clusters were present near Ni-enrichment. From the concentration maps, Figure 3-5(c), one Cu cluster is completely enveloped within a region of high Ni content while a second Cu cluster is partially enveloped in a region of higher Ni concentration. The higher concentration of Ni and its partitioning to crystalline phase prohibited a clear and spatially resolvable determination if the Cu clusters solely acted as a heterogeneous nucleation site for this ribbon.

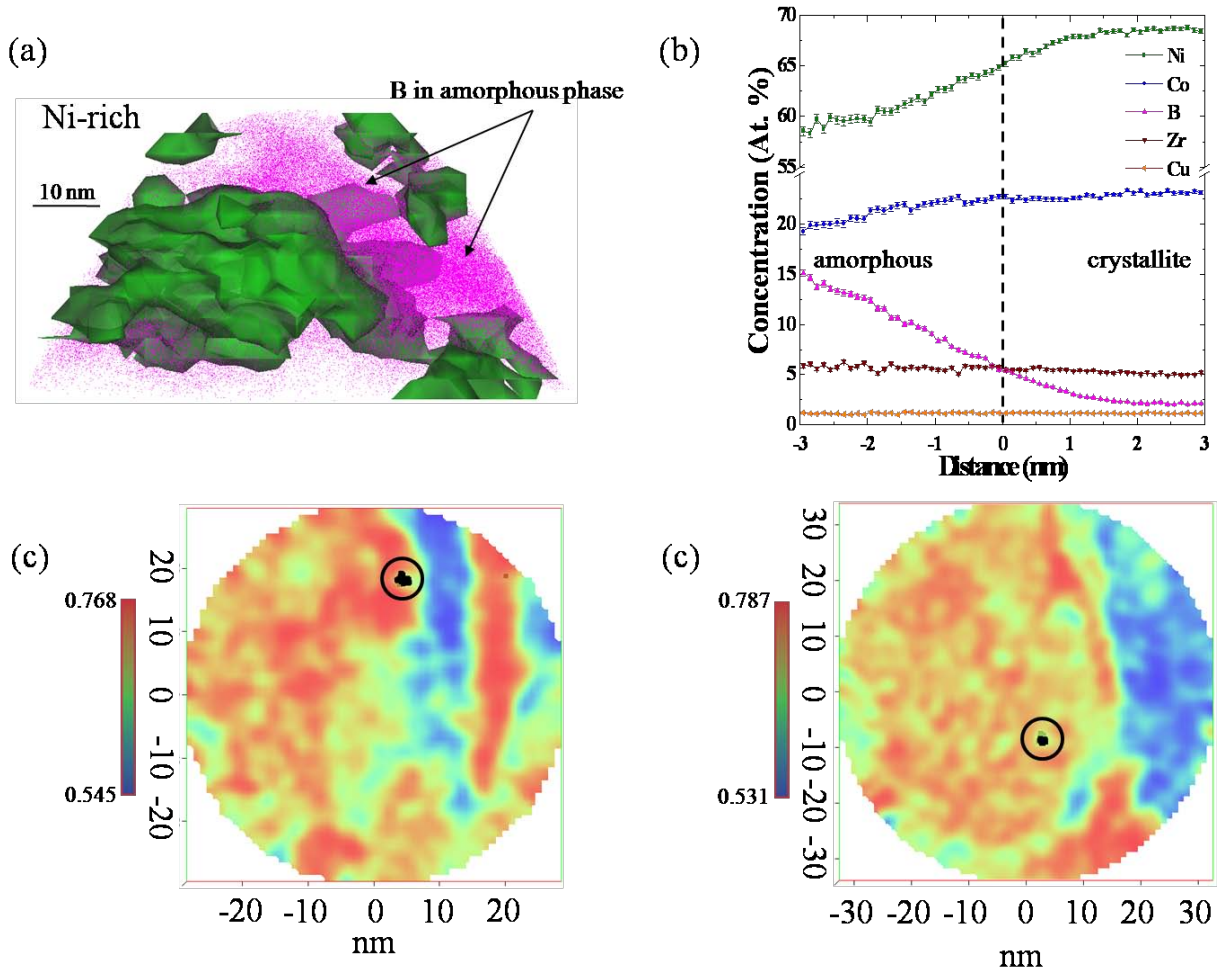


**Figure 3-5** (a) Ni isoconcentration surface (68.19 at.%) along with the B ions obtained from as-spun ( $\text{Co}_{0.25}\text{Ni}_{0.75}\text{B}_4\text{Cu}_1$ ) alloy. (b) Proximity histogram generated from the Ni isoconcentration surface (65.0 at.%) using a voxel size of 2.8 nm. (c) 2D concentration map of Ni content with two different Cu clusters encircled.

TEM micrographs for the T<sub>p</sub> annealed ribbons, Figure 3-6, of (Co<sub>0.75</sub>Ni<sub>0.25</sub>)<sub>88</sub>Zr<sub>7</sub>B<sub>4</sub>Cu<sub>1</sub> (X=0.25) and (Co<sub>0.25</sub>Ni<sub>0.75</sub>)<sub>88</sub>Zr<sub>7</sub>B<sub>4</sub>Cu<sub>1</sub> (X=0.75). The SAED pattern from the T<sub>p</sub> annealed (Co<sub>0.75</sub>Ni<sub>0.25</sub>)<sub>88</sub>Zr<sub>7</sub>B<sub>4</sub>Cu<sub>1</sub> (X=0.25) alloy ribbon, Figure 3-6(a), consisted of reflections from the matrix hcp phase, a Ni<sub>5</sub>Zr phase, and a diffuse halo ring associated with the amorphous phase. The latter ring indicates that full crystallization has not been completed. The bright field micrograph of Figure 3-6(b) showed fine scale hcp crystallites that are homogeneously dispersed within the matrix. The average grain size of these hcp crystallites was approximately 10 to 20 nm.

The SAD pattern of the T<sub>p</sub> annealed (Co<sub>0.25</sub>Ni<sub>0.75</sub>)<sub>88</sub>Zr<sub>7</sub>B<sub>4</sub>Cu<sub>1</sub> (X=0.75) ribbon, Figure 3-6(c), confirmed the XRD results that the main constituent phase is fcc. Additional ring patterns from the Ni<sub>5</sub>Zr were observed and are in agreement with the XRD phase identification. From the bright field micrograph in Figure 3-6(d), the average grain size of the crystallites was approximately 20 to 30 nm, which is slightly larger than the approximately 15 to 20 nm seen in the as-spun ribbon for the equivalent composition.

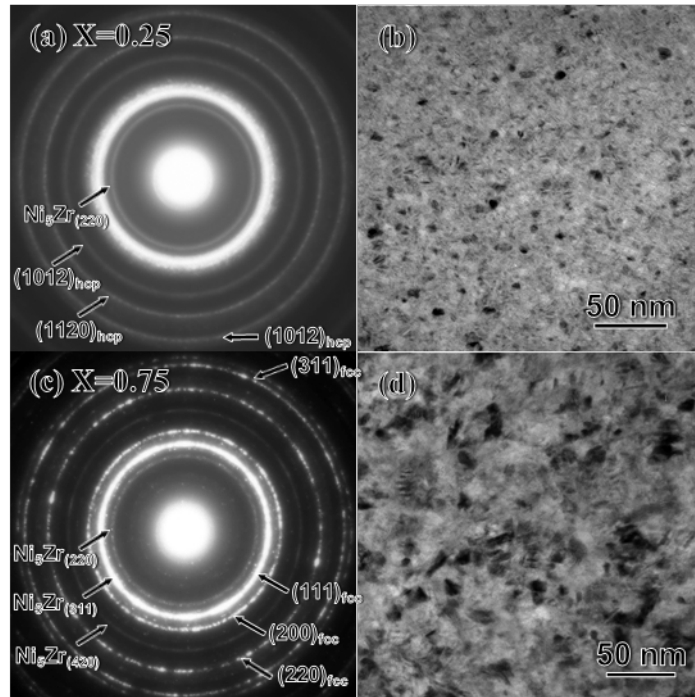


**Figure 3-6** (a) Selected area diffraction (SAD) pattern and (b) bright field TEM images of the T<sub>p</sub> annealed (Co<sub>0.75</sub>Ni<sub>0.25</sub>)<sub>88</sub>Zr<sub>7</sub>B<sub>4</sub>Cu<sub>1</sub> (X=0.25) alloy; and (c) Selected area diffraction (SAD) pattern and (d) bright field TEM images of the T<sub>p</sub> annealed (Co<sub>0.25</sub>Ni<sub>0.75</sub>)<sub>88</sub>Zr<sub>7</sub>B<sub>4</sub>Cu<sub>1</sub> (X=0.75) alloy.

The atom map reconstructions and proximity histogram from the annealed (Co<sub>0.75</sub>Ni<sub>0.25</sub>)<sub>88</sub>Zr<sub>7</sub>B<sub>4</sub>Cu<sub>1</sub> (X=0.25) alloy, Figure 3-7(a) and (b), revealed that the annealing process promoted further partitioning between the Co and Ni to the respective amorphous and crystalline phases, as compared to the previous ribbon's atom probe data set in Figure 3-4. Comparing the as-spun proxigram of Figure 3-4(b) to the annealed proxigram of Figure 3-7(b), the annealing process appeared to have had little effect on the slight partitioning of Zr to the Ni-enriched crystallite. The B partitioning also appeared to be nonexistent between the phases regardless of the annealing. As done previously, a clustering analysis of Cu was performed to determine any spatial correlation of the crystallization to the Cu present in the alloy. Figure 3-7(c)-(d) revealed two separate Cu clusters within the 2D concentration map for both Co and Ni.

The cluster in Figure 3-7(c) is in a nominal region of Co and Ni suggestive that it did not act as a preferential heterogeneous nucleation site for this composition. The second concentration map, Figure 3-7(d) revealed that the Cu cluster is in a nominal region of Co content, but the cluster is partially enveloped by a region of higher Ni content leaving any results ambiguous.

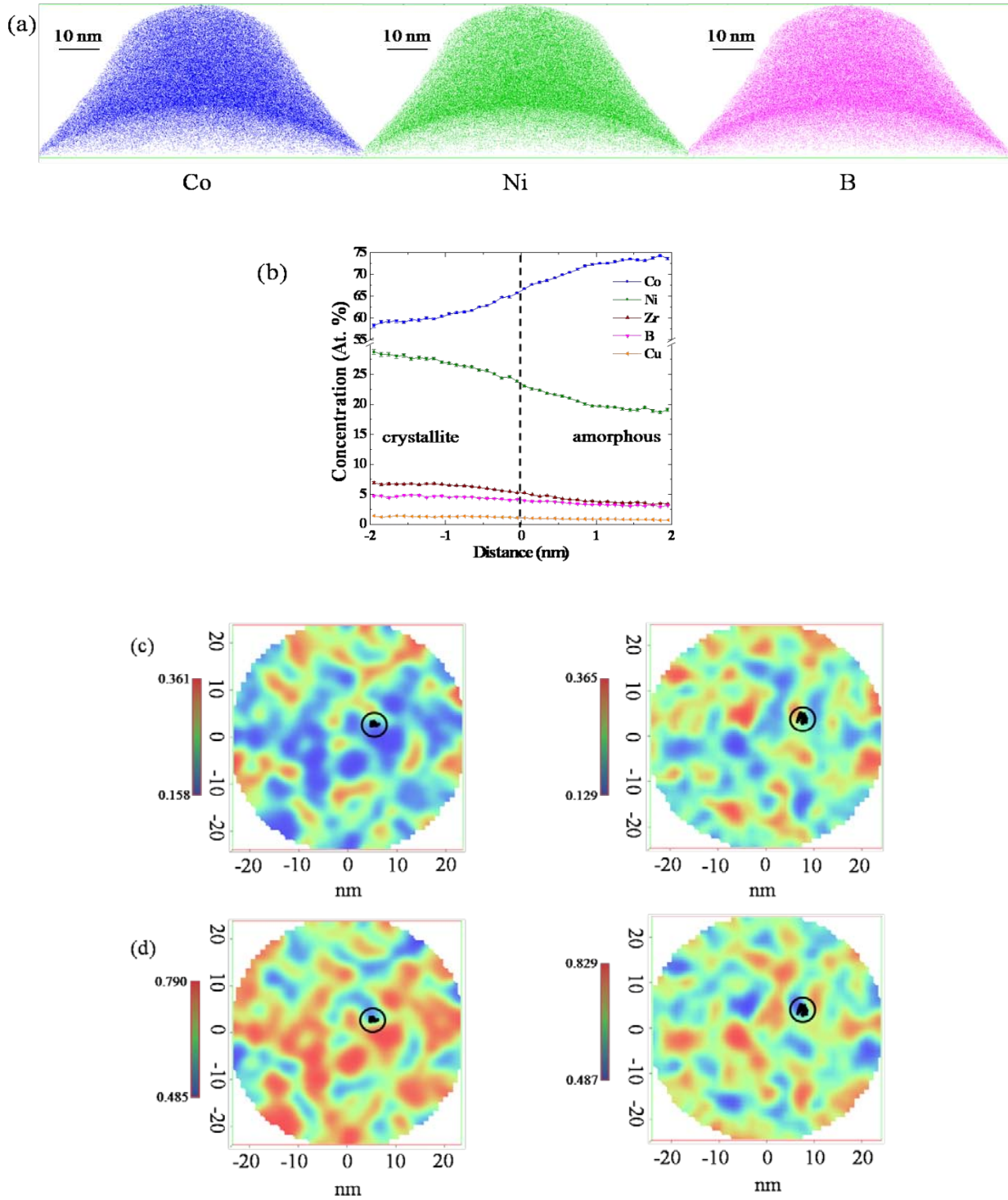


**Figure 3-7** (a) Ion maps of Co, Ni, and B from the annealed  $(\text{Co}_{0.75}\text{Ni}_{0.25})_{88}\text{Zr}_7\text{B}_4\text{Cu}_1$  ( $X=0.25$ ) atom probe tip. (b) Proximity histogram generated from the Co isoconcentration surface (66.18 at.%) using a voxel size of 1.8 nm. (c) 2D concentration map of Co and Ni content respectively with same Cu clusters encircled. (d) 2D concentration map of Co and Ni content respectively with second different Cu clusters encircled than in part (c).

The atom probe reconstructions from  $T_p$  annealed  $(Co_{0.25}Ni_{0.75})_{88}Zr_7B_4Cu_1$  ( $X=0.75$ ) alloy, Figure 3-8(a), confirmed further chemical partitioning of Ni, Co, and B between the phases as previously observed in the as-spun ribbon of the same composition. The slight Zr partitioning seen in Figure 3-8(b) is similar to all previous atom probe datasets; it showed a preference to the Ni-enriched crystallite phase. The Cu clustering overlaid with the 2D concentration map revealed that the Cu cluster is not present in a region of higher than nominal Ni, Figure 3-8(c), content suggesting that the Cu did not act as a preferential heterogeneous nucleation site for the Ni-rich crystalline precipitation.

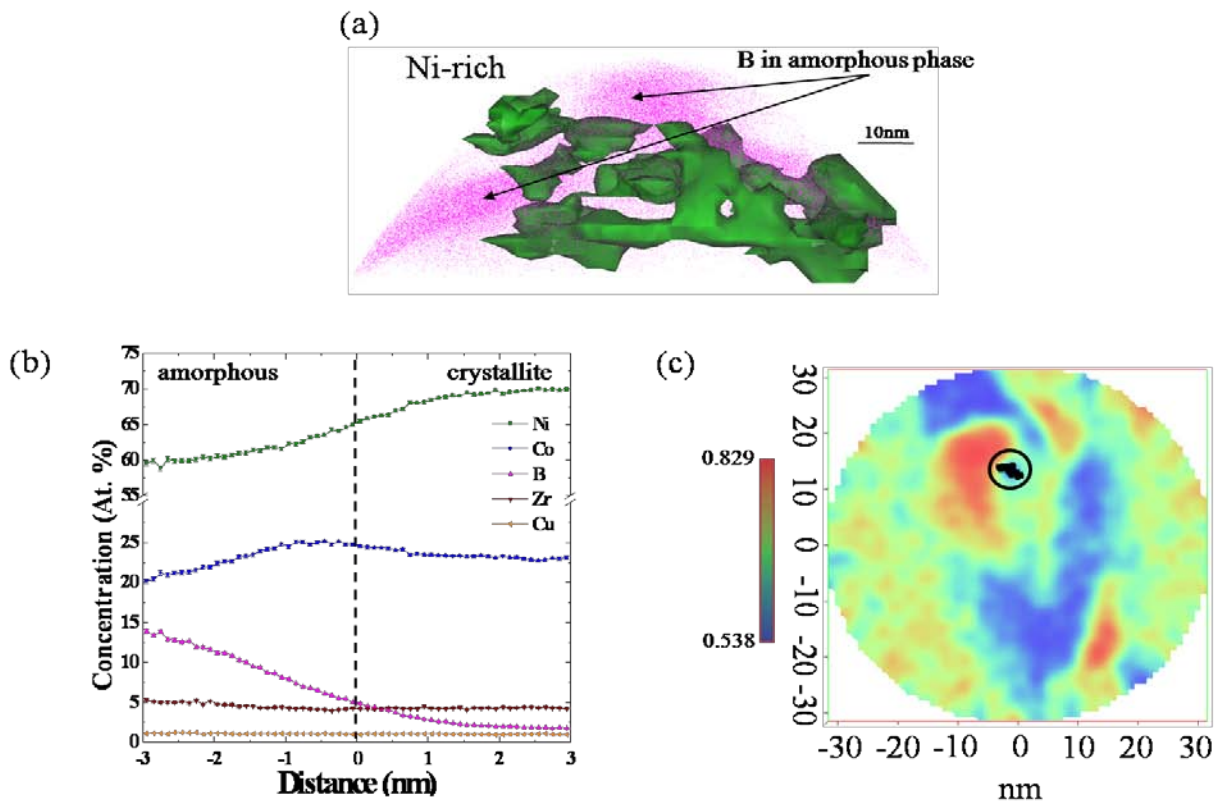


**Figure 3-8** (a) Ni isoconcentration surface (65.74 at.%) along with the B ions obtained from annealed  $(Co_{0.25}Ni_{0.75})_{88}Zr_7B_4Cu_1$  ( $X=0.75$ ) alloy using a voxel size is 2.5 nm for the analysis of this dataset. (b) Proximity histogram generated from the Ni isoconcentration surface (65.74 at.%). (c) 2D concentration map of Ni content with Cu cluster.

### 3.2.1 Transmission Electron Microscopy (TEM) and Atom Probe Tomography (ATP)

#### Discussion

The atom probe data sets for all compositions studied revealed a chemical partitioning of Ni to the crystallite phase; this is consistent with the Kissinger analysis that Ni promoted easier crystallization. For these particular crystallite phases, the crystal structure was determined by whether the Co or Ni was the dominate composition. This is consistent with the binary Co-Ni phase diagram [41], where Co-rich alloys are hcp-based phases and Ni-rich alloys are fcc-based phases.

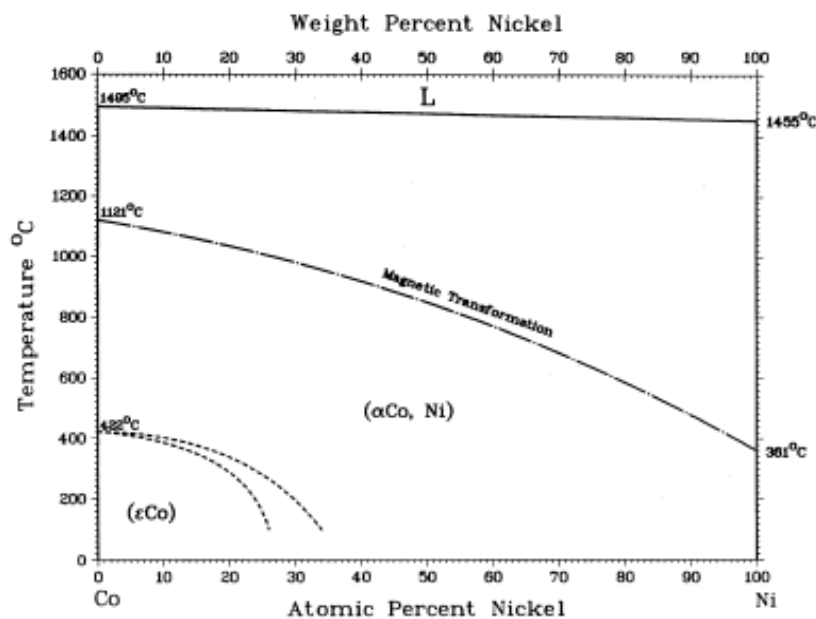


**Figure 3-9** The Nickel-Cobalt binary phase diagram.

In terms of the crystallization kinetics, the Cu clusters did not appear to significantly influence the spatial precipitation behavior for any alloys characterized; this was manifested by relative insensitivity of Cu concentration between the phases in the atom probe derived proximity histograms in Figures 3-4(b), 3-5(b), 3-6(b), and 3-7(b) as well as the 2D compositional spatial maps with the overlay of the cluster location. If Cu were a heterogeneous nucleation site, its impact would have an even greater impact in the as-spun  $(Co_{0.75}Ni_{0.25})_{88}Zr_7B_4Cu_1$  ( $X=0.25$ ) Ni-lean alloy with its slower kinetics as compared to the as-spun  $(Co_{0.25}Ni_{0.75})_{88}Zr_7B_4Cu_1$  ( $X=0.75$ ) Ni-rich alloy with its faster kinetics. This was not observed in the atom probe data sets. Since the Cu clusters played no role as a nucleation site for the as-spun version, it seemed highly unlikely that it would give any additional, favorable energy considerations for the annealing process and subsequent crystallite nucleation. Moreover, the  $\Delta H_{mix}$  for Cu-Co and Cu-Ni are 6 and 4 kJ/mol [42] respectively; both of which are slightly endothermic or unfavorable conditions. Thus, for these alloys, the major chemical character of the ribbon, Co verses Ni, was more dominate on promoting crystallization than the heterogeneous cluster site engineering concepts, as previously discussed in the literature [21-23]. Consideration of the  $\Delta H_{mix}$  for the constitute elements should also be considered if such elements can thermodynamically mix and promote heterogeneous nucleation.

Upon crystallization, the crystallite sizes scaled with increasing Ni-content. Clearly, the easier to crystallize allowed easier growth for the crystallites. In terms of the other microalloyed elements, Zr is thought to inhibit grain growth through Zener pinning and/or by acting as a diffusion barrier [19]. The atom probe data, Figures 3-4(b), 3-5(b), 3-6(b), and 3-7(b), for all the alloys revealed Zr partitioned slightly more with Ni. The  $\Delta H_{mix}$  for Zr-Ni and Zr-Co are -49 and

-41 kJ/mol [42] respectively. Since both are exothermic and favorable reactions, with the Zr-Ni are being somewhat more energetically favorable, this explains the slight enrichment observed. In the Co-rich compositions, this Zr elemental separation to the crystallite was intensified in comparison to the Ni-rich composition since the Ni content was more strongly partitioned. In all cases, the Zr did not partition to the grain boundaries. Thus its ability to inhibit grain growth of Ni crystallites would be limited to a role as a diffusion barrier rather than a Zener pinning mechanism.

In the Co-rich alloy ( $X=0.25$ ), B did not preferentially segregate to either the amorphous or crystalline phases, Figures 3-4 and 3-7. The  $\Delta H_{mix}$  for Co-B and Ni-B are both approximately -9 kJ/mol, respectively. In contrast, the Ni-rich alloys' ( $X=0.75, 1.0$ ) strong B segregation was noted in Figures 3-5 and 3-8. Boron's partitioning does not seem to be primarily controlled by the  $\Delta H_{mix}$  since Co-B and Ni-B have approximately identical values. The increased Ni content must have caused a switch in the dominating thermodynamic behavior for B that resulted in the noticeable segregation of B to the grain boundary and/or amorphous regions.

First, Zr is a much more favorable mixing reaction with Ni, *i.e.* Ni-Zr  $\Delta H_{mix}$  is -49 kJ/mol compared to Ni-B  $\Delta H_{mix}$  of -9 kJ/mol. Second, B is a known glass stabilizer [1], which may account for its preference to reside in the boundaries or amorphous regions that have not yet crystallized in the as-spun or annealed condition. This type of B segregation to the grain boundaries and/or amorphous regions is constant with Ping *et al.* and Ohodnicki *et al.* observations in Co:Fe alloys [22,43].

### 3.3 Magnetic Measurements Results

Figure 3-9(a) and (b) shows the variation in saturation magnetization and coercivity as a function of Ni content. The saturation magnetization of the ribbons decreased by over 80% as the Ni content increased. The coercivity increased as the Ni content increased for both as-spun and annealed ribbons. The only exception from this trend was the Co-rich ( $X=0.25$ ) alloy. At each composition, annealing did result in a slight increase in the coercivity value.

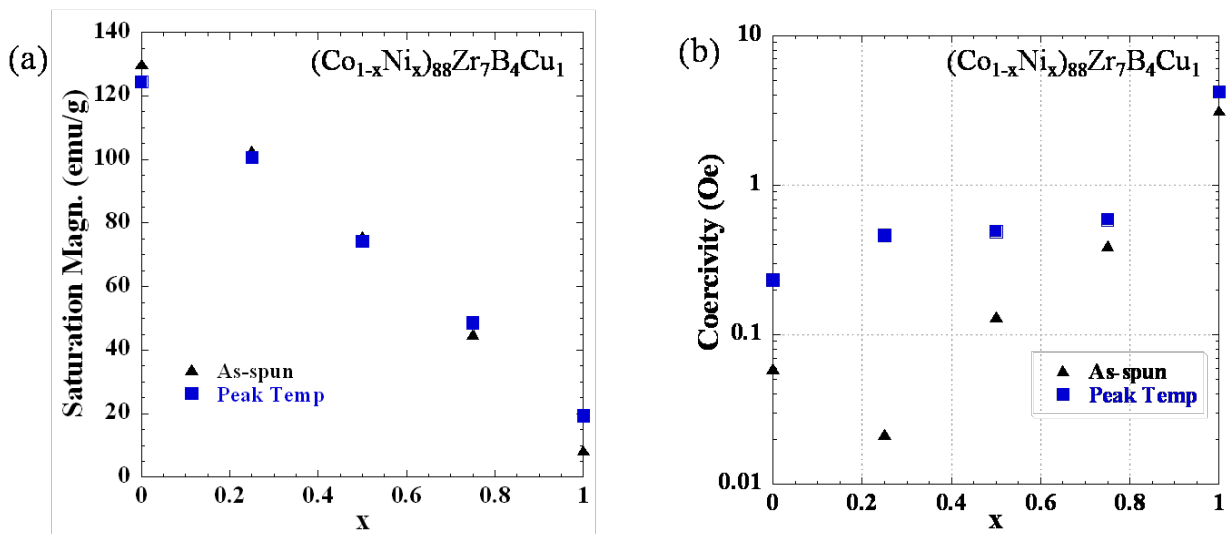


**Figure 3-10** (a) Saturation magnetization versus increasing Ni content ( $X$ ). (b) Coercivity versus increasing Ni content ( $X$ ).

### 3.3.1 Magnetic Measurement Discussion

From Figure 3-9(a), the saturation magnetization decreased with increasing Ni content. This would be expected since Ni has a lower moment than Co [44]. In the amorphous state, the magnetic domains are crystallographically not defined which could make them more difficult to saturate [7]. Upon crystallization, it can become easier to saturate these crystalline domains. Unfortunately, annealing the Ni-rich ribbon, with various minor alloying elements, can result in the precipitation and growth of extraneous intermetallics like  $\text{Ni}_5\text{Zr}$  which alter the saturation values compared to elemental Ni [45].

Finally, the coercivity increased for all composition with annealing, Figure 3-9(b). This is contributed to the crystallization and increase in grain size with annealing. As noted by Herzer [7,9], coercivity increases with grain size up to approximately 100 nm for these nanocrystalline alloys. This behavior occurs because the domain wall's thickness exceeds the grain size, thus the domain wall samples several grains so that fluctuations in magnetic anisotropy that are on the grain size length scale are irrelevant to domain wall pinning [1]. The Ni rich alloys, in general had larger coercivity values because of their larger grain sizes.

## Chapter 4 Conclusion

### 4.1 Major Findings

A series of melt-spun ribbons with a composition  $(Co_{1-X}Ni_X)_{88}Zr_7B_4Cu_1$ , where X varied from 0 to 1, were melt spun and resulted in the following conclusions:

- By increasing Ni content in the  $(Co_{1-X}Ni_X)_{88}Zr_7B_4Cu_1$  alloy, a decrease in magnetic saturation, an increase in coercivity, and a promotion of crystallization (even in as-spun condition with the cooling rates of  $\sim 10^6$  °C/s) occurred.
- Atom probe tomography revealed partitioning of Ni to the crystallites whereas Co trended with the amorphous phase.
- Atom probe tomography indicated that Cu did form clusters, but these clusters did not act as heterogeneous nucleation sites for crystallization; rather the Co: Ni chemical composition was dominate and  $\Delta H_{mix}$  not favorable. This was in agreement with the Kissinger analysis which showed a reduction in the crystallization activation energy with increasing Ni content.
- Atom probe tomography indicated Zr did not partition to the grain boundaries and has been explained in terms of the enthalpy of mixing energies. Therefore it could not serve as a Zener-pinning grain growth impeding mechanism.

- B segregated to the amorphous regions for the Ni-rich alloys ( $X=0.75$  &  $1.0$ ). This has been contributed to its role as a glass forming additive and is one of the last elements to partition to the Ni-rich crystalline phase.
- No B segregation was observed in the Co-rich alloy ( $X=0.25$ ), which were amorphous in the as-spun state.

#### 4.2 Future Work

Future work can focus on further establishing the relationship between additional magnetic properties and microstructural evolution moving from  $X=0$  to  $1$ . Some suggested topics are:

- Using the Co:Ni APT analysis approach with respect to enthalpy mixing energies, revisit the Fe:Co alloys to determine if Cu clustering could be considered a thermodynamically favorable nucleation sites.
- Investigate how the Curie temperature is affected by the changing composition in Co:Ni.
- Determine the role the phases play in decreasing or increasing the Curie temperature for the different ribbon compositions.

## Chapter 5      References

- [1] M.E. McHenry, M.A. Willard, & D.E. Laughlin, “Amorphous and nanocrystalline materials for applications as soft magnets.” Progress in Materials Science 44 (1999): 291-433.
- [2] R. Grossinger & R.S. Turtelli, “Bulk Nanocrystalline and Amorphous Magnetic Materials.” Bulk Nanostructured Materials. 27 (2009):605-633.
- [3] H.A. Davies, *Amorphous Metallic Alloys*, F.E. Luborsky (ed.) Butterworths, London, (1983) pp. 8.
- [4] R. Hasegawa, *Glassy Metals: Magnetic, Chemical and Structural Properties*, CRC Press, Boca Raton, Fl, (1982).
- [5] T. Matsumoto, I. Ohnaka, A. Inoue, & M. Hagigawa, *Scr. Metal.* 15, 293 (1981).
- [6] H. Gavrila & V. Ionita, “Crystalline and Amorphous Soft Magnetic Materials and Their Applications - Status of Art and Challenges.’ Journal of Optoelectronics and Advanced Materials. Vol.4 (#2) (2002):173-192.
- [7] G. Herzer. “Grain Size Dependence of Coercivity and Permeability in Nanocrystalline Ferromagnets.” IEEE Transaction on Magnetics Vol. 26 (#5) (1990): 1397-1402.
- [8] G. Herzer, “Magnetization process in nanocrystalline ferromagnets.” Materials Science and Engineering. A133 (1991):1-5.
- [9] G. Herzer, “Nanocrystalline soft magnetic materials.” Journal of Magnetism and Magnetic Materials 112 (1992): 258-262.
- [10] M.A. Willard & M. Daniil, “13. Nanostructured Soft Magnetic Materials,” Nanoscale Magnetic Materials and Applications. Springer: New York, 2008. 1-30.
- [11] Y. Yoshizawa, K. Yamauchi, T. Yamane, H. Sugihara. “Common-Mode Choke Cores Using the New Fe-Based Alloys Composed of Ultrafine Grain-Structure.” Journal of Applied Physics. Vol.64 (#10) (1988):6047-9.
- [12] Y. Yoshizawa & K. Yamauchi, “Effects of Magnetic-Field Annealing on Magnetic Properties in Ultrafine Crystalline Fe-Cu-Nb-Si-B Alloys.” IEEE Transactions on Magnetics. Vol.25(#5) (1989):3324-6.

- [13] Y. Yoshizawa, S. Oguma, & K. Yamauchi, "New Fe-Based Soft Magnetic-Alloys Composed of Ultrafine Grain-Structure." Journal of Applied Physics. Vol.64(#10) (1988):6044-6.
- [14] K. Suzuki, M. Kikuchi, A. Makino, A. Inoue, & T. Masumoto, "Changes in Microstructure and Soft Magnetic-Properties of an Fe<sub>86</sub>Zr<sub>7</sub>B<sub>6</sub>Cu<sub>1</sub> Amorphous Alloy Upon Crystallization." Materials Transactions JIM. Vol.32(#10) (1991):961-8.
- [15] M.A. Willard, D.E. Laughlin & M.E. McHenry, "Structure and magnetic properties of (Fe<sub>0.5</sub>Co<sub>0.5</sub>)<sub>88</sub>Zr<sub>7</sub>B<sub>4</sub>Cu<sub>1</sub> nanocrystalline alloys." Journal of Applied Physics. Vol. 84 (#12) (1998): 6773-7.
- [16] M. Muller, H. Grahl, N. Mattern, U. Kuhn, & B. Schnell, "The influence of Co on the structure and magnetic properties of nanocrystalline FeSiB-CuNb and FeZrBCu-based alloys." Journal of Magnetism and Magnetic Materials. 160 (1996):284-6.
- [17] Z. Gercsi, F. Mazaleyrat, & L.K. Varga, "High-temperature soft magnetic properties of Co-doped nanocrystalline alloys." Journal of Magnetism and Magnetic Materials. Vol.302(#2) (2006):454-8.
- [18] C. Gomez-Polo, J.I. Perez-Landazabal, & V. Recarte, "Temperature dependence of magnetic properties in Fe-Co and Fe-Cr base nanocrystalline alloys." IEEE Transactions on Magnetics. Vol.39(#5)(2003):3019-24.
- [19] M.E. McHenry, F. Johnson, H. Okumura, T. Ohkubo, V.R.V. Ramanan, & et al. "The kinetics of nanocrystallization and microstructural observations in FINEMET, NANOPERM, and HITPERM nanocomposite magnetic materials." Scripta Materialia 48 (2003): 881-887.
- [20] M.A. Willard, J.C. Claassen, R.M. Stroud, T.L. Francavilla & V.G. Harris, "(Ni,Fe,Co)-Based Naoncrystalline Soft Magnets With Near-Zero Magnetostriction." IEEE Transactions on Magnetics. Vol. 38 (#5) (2002): 3045-50.
- [21] C.F. Conde, A. Conde, P. Svec, & P. Ochin, "Influence of the addition of Mn and Cu on the nanocrystallization process of HITPERM Fe-Co-Nb-B alloys." Materials Science and Engineering A (2004): 718-721.
- [22] D.H. Ping, Y.Q. Wu, K. Hono, M.A. Willard, M.E. McHenry, & et al. "Microstructural characterization of (Fe<sub>0.5</sub>Co<sub>0.5</sub>)<sub>88</sub>Zr<sub>7</sub>B<sub>4</sub>Cu<sub>1</sub> nanocrystalline alloys" Scripta Materialia 45 (2001): 781-786.
- [23] Y. Yoshizawa, S. Fujii, D.H. Ping, M. Ohnuma, & K. Hono, "Magnetic properties of nanocrystalline FeMCuNbSiB alloys (M: Co, Ni)." Scripta Materialia 48 (2003): 863-868.
- [24] O. Knotelc, F. Jungblut & A. Barimani, "On the Stability of Hetastable and Amorphous Pvd-Compound Films." MRS Proceedings, 157 (1989): 859.

- [25] B.E. White Jr., M.E. Patt, & E. J. Cotts, “Comparison of solid-state amorphization reactions in deformed Ni-Ti and Ni-Zr multilayered composites.” PHYSICAL REVIEW B. Vol. 42 (#17) (1990): 11017-27.
- [26] R. Brunetto1, G.A. Barattaz, & G. Strazzulla, “Amorphization of diamond by ion irradiation: a Raman study.” Institute of Physics Publishing Journal of Physics: Conference Series 6 (2005): 120–125.
- [27] H.M. Wu, C.J. Hu, & H.C. Li, “Formation of Co-Fe-M-B (M=Zr, Ti) amorphous powders by mechanical alloying and their magnetic properties.” Journal of Alloys and Compounds. 483 (2009): 553-556.
- [28] H. Kissinger: Anal. Chem., 1957, vol. 29 , pp. 1702–06.
- [29] Z.L. Wang, “New Developments in Transmission Electron Microscopy for Nanotechnology.” Advanced Materials. Vol.15 (#18) (2003): 1497-1514.
- [30] M. K. Miller, Atom Probe Tomography: Analysis at the atomic level Kluwer Academic/Plenum Publishers, New York (2000).
- [31] A. Cerezo, D. J. Larson, & G. D. W. Smith “Progress in the atomic-scale analysis of materials with three-dimensional atom probe”, MRS Bulletin Vol.26 (#2) (2001) 102-107.
- [32] T.F. Kelly, T.T. Gribb, J.D. Olson, R.L. Martens, J.D. Shepard, S.A. Wiener, T.C. Kunicki, R.M. Ulfig, D.R. Lenz, E.M. Strennen, E. Oltman, J.H. Bunton, & D.R. Strait "First Data from a Commercial Local Electrode Atom Probe (LEAP)" Microscopy and Microanalysis. Vol.10 (2004) 373-383.
- [33] M.K. Miller & R.G. Forbes “Atom probe tomography” Materials Characterization. 60, (2009): 461-469.
- [34] D. N. Siedman, “Three-Dimensional Atom-Probe Tomography: Advances and Applications.” Annual Review of Materials Research. Vol. 37 (2007):127-158.
- [35] M.K. Miller, A. Cerezo, M.G. Hetherington, & G.D.W. Smith, Atom Probe Field Ion Microscopy, Clarendon Press, Oxford, 1996.
- [36] K.L. Torres, M. Daniil, M.A. Willard, & G.B. Thompson, “The influence of voxel size on atom probe tomography data.” Ultramicroscopy 111 (2011): 464-468.
- [37] G.B. Thompson, M.K. Miller, & H.L Fraser, “Some aspects of atom probe specimen preparation and analysis of thin film materials.” Ultramicroscopy 100 (2004): 25-34.
- [38] L.A. Giannuzzi, Microscopy and Microanalysis Proceedings. 12 (2006): 1260.

- [39] K. Thompson, D. Lawrence, D.J. Larson, J.D. Olson, T.F. Kelly, B. Gorman, Ultramicroscopy 107 (2007): 131-139.
- [40] J.M Hyde & C.A. English, “An analysis of the structure of irradiation induced Cu-enriched clusters in low and high nickel welds, in MRS 2000 Fall Meeting, Symposium R: Microstructural Processes in Irradiated Materials.” Vol. 650, Materials Research Society, Boston, MA, 2000, pp. R6.6.1-R6.612.
- [41] H. Baker. “Alloy Phase Diagrams.” ASM Handbook Vol. 3. ASM International, 1992. 145.
- [42] F.R. de Boer & *et al.* “Cohesion in Metals” Transition Metal Alloys. Elsevier Science Publishers. 1988.
- [43] P.R. Ohodnicki Jr., Y.L. Qin, D.E. Laughlin, M.E. McHenry, M. Kodzuka, & et al. “Composition and non-equilibrium crystallization in partially devitrified co-rich soft magnetic nanocomposite alloys.” Acta Materialia 57 (2009): 87-96.
- [44] J.M. MacLaren, T.C. Schulthess, W.H. Butler, R.A. Sutton, & M.E. McHenry, J Appl Phys. 1999;85:4833.
- [45] A. Amamou, R. Kuentzler, Y. Dossmann, P. Forey, J.L. Glimois, & et al. “Electronic structure and electron-phonon coupling in the Ni-Zr system.” Journal of Physics F-Metal Physics 12 (1982): Issue 11, 2509-2522.

Chapter 6      Appendix

CH001 x=0						Final Wt.	Final Wt.
Element	At. %	At. Weight	Wt %	Mass (g)	pre-melt (g)	post-melt (g)	Wt% change
Ni	0.00	58.70	0.00	0.00	0.00	weight before melt spinning (g)	0.063
Co	88.00	58.93	87.43	20.40	20.40		
Zr	7.00	91.22	10.77	2.51	2.51		
Nb	0.00	92.91	0.00	0.00	0.00		
B	4.00	10.81	0.73	0.17	0.17		
Cu	1.00	63.55	1.07	0.25	0.25		
<b>Total</b>	100.00	5931.17	100.00	23.33	23.33	23.31	22.30
CH002 x=0.25						Final Wt.	Final Wt.
Element	At. %	At. Weight	Wt %	Mass (g)	pre-melt (g)	post-melt (g)	Wt% change
Ni	22.00	58.70	21.79	5.06	5.06	weight before melt spinning (g)	0.014
Co	66.00	58.93	65.63	15.23	15.23		
Zr	7.00	91.22	10.78	2.50	2.50		
Nb	0.00	92.91	0.00	0.00	0.00		
B	4.00	10.81	0.73	0.17	0.17		
Cu	1.00	63.55	1.07	0.25	0.25		
<b>Total</b>	100.00	5926.11	100.00	23.20	23.20	23.20	22.08
CH003 x=0.5						Final Wt.	Final Wt.
Element	At. %	At. Weight	Wt %	Mass (g)	pre-melt (g)	post-melt (g)	Wt% change
Ni	44.00	58.70	43.62	10.11	10.11	weight before melt spinning (g)	0.078
Co	44.00	58.93	43.79	10.15	10.15		
Zr	7.00	91.22	10.78	2.50	2.50		
Nb	0.00	92.91	0.00	0.00	0.00		

<b>B</b>	4.00	10.81	0.73	0.17	0.17		<b>weight before</b>
<b>Cu</b>	1.00	63.55	1.07	0.25	0.25		<b>melt spinning (g)</b>
<b>Total</b>	100.00	5921.05	100.00	23.19	23.19	23.17	22.47
<b>CH004 x=0.75</b>							
Element	At. %	At. Weight	Wt %	Mass (g)	pre-melt (g)	post-melt (g)	Wt% change
<b>Ni</b>	66.00	58.70	65.49	15.83	15.83		0.017
<b>Co</b>	22.00	58.93	21.91	5.30	5.30		
<b>Zr</b>	7.00	91.22	10.79	2.61	2.61		
<b>Nb</b>	0.00	92.91	0.00	0.00	0.00		
<b>B</b>	4.00	10.81	0.73	0.18	0.18		<b>weight before</b>
<b>Cu</b>	1.00	63.55	1.07	0.26	0.26		<b>melt spinning (g)</b>
<b>Total</b>	100.00	5915.99	100.00	24.17	24.17	24.17	23.25
<b>CH005 x=1.00</b>							
Element	At. %	At. Weight	Wt %	Mass (g)	pre-melt (g)	post-melt (g)	Wt% change
<b>Ni</b>	88.00	58.70	87.39	20.94	20.94		0.005
<b>Co</b>	0.00	58.93	0.00	0.00	0.00		
<b>Zr</b>	7.00	91.22	10.80	2.59	2.59		
<b>Nb</b>	0.00	92.91	0.00	0.00	0.00		
<b>B</b>	4.00	10.81	0.73	0.18	0.18		<b>weight before</b>
<b>Cu</b>	1.00	63.55	1.08	0.26	0.26		<b>melt spinning (g)</b>
<b>Total</b>	100.00	5910.93	100.00	23.96	23.96	23.96	22.88

**Appendix 6-1** Weight conversions, final weights, and percent change for all compositions.